

PAPER

Design of a digital phantom population for myocardial perfusion SPECT imaging research

To cite this article: Michael Ghaly *et al* 2014 *Phys. Med. Biol.* **59** 2935

View the [article online](#) for updates and enhancements.

You may also like

- [Task-based evaluation of a 4D MAP-RBL-EM image reconstruction method for gated myocardial perfusion SPECT using a human observer study](#)
Taek-Soo Lee, Takahiro Higuchi, Riikka Lautamäki et al.
- [A study of myocardial perfusion SPECT imaging with reduced radiation dose using maximum likelihood and entropy-based maximum *a posteriori* approaches](#)
N V Denisova and I N Terekhov
- [Optimization and comparison of simultaneous and separate acquisition protocols for dual isotope myocardial perfusion SPECT](#)
Michael Ghaly, Jonathan M Links and Eric C Frey

Introducing SunCHECK® 5.0

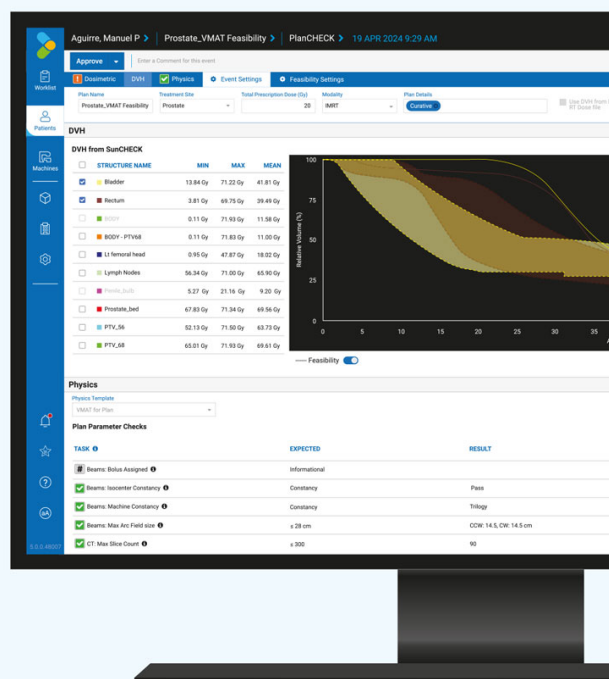
The Connected Workspace
for Higher Quality



What's New

- Simple and clean UI
- Plan quality assessment
- Expanded QA device control

Get a demo in ASTRO booth #1427



Design of a digital phantom population for myocardial perfusion SPECT imaging research

Michael Ghaly¹, Yong Du¹, George S K Fung¹,
Benjamin M W Tsui¹, Jonathan M Links² and Eric Frey¹

¹ The Russell H Morgan Department of Radiology and Radiological Science,
Johns Hopkins University, Baltimore, MD, USA

² Department of Environmental Health Sciences, Johns Hopkins University,
Baltimore, MD, USA

E-mail: mghaly@jhu.edu

Received 16 October 2013, revised 24 March 2014

Accepted for publication 8 April 2014

Published 19 May 2014

Abstract

Digital phantoms and Monte Carlo (MC) simulations have become important tools for optimizing and evaluating instrumentation, acquisition and processing methods for myocardial perfusion SPECT (MPS). In this work, we designed a new adult digital phantom population and generated corresponding Tc-99m and Tl-201 projections for use in MPS research. The population is based on the three-dimensional XCAT phantom with organ parameters sampled from the Emory PET Torso Model Database. Phantoms included three variations each in body size, heart size, and subcutaneous adipose tissue level, for a total of 27 phantoms of each gender. The SimSET MC code and angular response functions were used to model interactions in the body and the collimator-detector system, respectively. We divided each phantom into seven organs, each simulated separately, allowing use of post-simulation summing to efficiently model uptake variations. Also, we adapted and used a criterion based on the relative Poisson effective count level to determine the required number of simulated photons for each simulated organ. This technique provided a quantitative estimate of the true noise in the simulated projection data, including residual MC simulation noise. Projections were generated in 1 keV wide energy windows from 48–184 keV assuming perfect energy resolution to permit study of the effects of window width, energy resolution, and crosstalk in the context of dual isotope MPS. We have developed a comprehensive method for efficiently simulating realistic projections for a realistic population of phantoms in the context of MPS imaging. The new phantom population and realistic database of simulated projections will be useful in performing mathematical

and human observer studies to evaluate various acquisition and processing methods such as optimizing the energy window width, investigating the effect of energy resolution on image quality and evaluating compensation methods for degrading factors such as crosstalk in the context of single and dual isotope MPS.

Keywords: digital phantom population, myocardial perfusion SPECT, Monte Carlo simulation

1. Introduction

Myocardial perfusion SPECT (MPS) has been shown to be an accurate and useful non-invasive diagnostic imaging technique for the detection and functional characterization of coronary artery disease, and is one of the most commonly performed nuclear medicine imaging procedures. While there have been advances in cardiac imaging with modalities such as MRI and CT angiography, MPS continues to be a useful, widely used, and cost-effective diagnostic test to assess perfusion status.

Recent advances in MPS technology aim at reducing radiation exposure, improving image quality, increasing patient comfort and increasing clinical throughput. This includes the use of cameras with novel detector materials (including solid-state detectors such as cadmium zinc telluride (CZT)), novel camera geometries and collimator designs, new reconstruction and processing methods, and protocols that allow reduced imaging time. Of potential appeal is the use of a simultaneous stress Tc-99m/rest Tl-201 dual isotope cardiac SPECT protocol, which would allow for reduction in imaging time and associated increase in patient comfort, more accurate registration of the two scans, and an increase in clinical throughput.

In order to fully exploit these advances, it is essential to have tools that can be used for MPS system optimization and evaluation. However, due to radiation concerns and difficulty in obtaining true perfusion status, it is impractical to optimize the large number of imaging parameters with human or animal studies on clinically relevant tasks. It is equally impractical to perform optimization studies using physical phantoms, since they cannot realistically duplicate the organ shapes and spatial relationships of patients, and it is prohibitively expensive to fabricate populations of physical phantoms modeling a realistic range of patient sizes, variations, and deformations.

Computer generated digital phantoms offer a practical alternative approach to evaluate, compare, and improve medical imaging devices and techniques. In order for digital phantoms to reach their full potential as a research and evaluation tool, it is essential for them to be as anatomically realistic as possible. Otherwise, studies using them would not be indicative of what would occur in live patients.

The three-dimensional (3D) eXtended CArdiac Torso (XCAT) phantom, as well as its predecessor, the Nurbs-based CArdiac Torso (NCAT) phantom, have been widely used for medical imaging simulation (LaCroix *et al* 2000, Segars *et al* 2001, Segars and Tsui 2002, Funk *et al* 2006, Segars and Tsui 2009, Segars *et al* 2010, Fung *et al* 2010). The 3D XCAT and NCAT phantoms provide an accurate, realistic and flexible model of the human anatomy by using non-uniform rational B-splines NURBS surfaces. The XCAT models whole body male and female anatomies based on the 3D visible human male and female anatomical imaging data sets from the National Library of Medicine (NLM). With its basis upon human data and the inherent flexibility of the NURBS surfaces that allows transformation to model varying

patient anatomy, the XCAT is capable of creating a realistic population of patients of varying anatomy from which to perform myocardial perfusion SPECT imaging research.

In this work, we designed a new adult digital phantom population based on the 3D XCAT phantom. The population consists of fifty-four digital phantoms including variability in gender, body size, heart size and fat level. To realistically model anatomical variability in a way that is clinically relevant, we used anatomical distributions obtained from the Emory Cardiac Database (Barclay *et al* 2005). We chose particular parameters to vary based on those that have the biggest impact on MPS image quality. Of importance, we chose to model specific patient and organ sizes, rather than taking random samples from an assumed normal distribution (He *et al* 2004), in order to more uniformly span a range of meaningful patient sizes rather than to model a specific phantom population. Using these specific sizes, it is possible to see if methods fail for certain kinds of patients (e.g., very large or small). It is also possible to explore the dependence of optimal acquisition or reconstruction parameters on patient anatomy. This is potentially useful since it is something that can be observed prior to imaging.

In addition to accurately and realistically modeling patient populations, an accurate and realistic simulation of the imaging process is also essential. However, realistically modeling the imaging process is computationally demanding. We thus used several techniques to efficiently simulate realistic projections of the phantom population.

The first technique was to use an efficient simulation method. Monte Carlo (MC) methods have been extensively used in the field of nuclear medicine and emission tomography to model the various physical processes and instrumentation. A number of MC simulation tools have been developed that offer tradeoffs between simulation accuracy and flexibility on one hand and computation time on the other hand. The Simulation System for Emission Tomography (SimSET) is a widely used package, developed, validated, and maintained by the University of Washington Imaging Research Laboratory, which is specifically designed for the simulation of SPECT and PET using voxelized phantoms (Lewellen *et al* 1998). SimSET incorporates variance reduction techniques that are appropriate for nuclear medicine simulations and which greatly increase the simulation efficiency. SimSET models the important physical phenomena, including photoelectric absorption, Compton's scattering and coherent scattering. However, in SimSET, the collimator is not modeled using MC photon tracking, but by an approximate analytical model that neglects physical effects such as photon penetration, x-rays fluorescence, and scatter in the collimator. For some applications, such as dual isotope imaging using Tc-99m and Tl-201, septal Pb x-rays are detected in the Tl-201 photopeak energy window, this fluorescence x-ray component is a non-negligible degrading factor; discarding its effect in the simulation may lead to inaccurate results.

Full MC simulation of the collimator-detector system is computationally expensive and is impractical for the simulation of SPECT data, especially for studies involving populations of phantoms. Song *et al* (2005) developed and implemented a fast and accurate method to model collimator and detector effects based on angular response functions (ARFs). The ARF is a function of the incident photon's direction and energy and describes the probability that a photon traveling in a certain direction will interact with the collimator-detector system and be detected in an energy window of interest. The ARF tables are pre-computed using full MC simulations of a point source in air and are used subsequently to model the response of the detection system for a given energy deposition window.

In this work, we used ARF tables in conjunction with the SimSET MC code to efficiently and accurately model the interactions in the patient and collimator-detector system, respectively. In this method, the photon interactions inside the phantom are modeled using SimSET. When the photon exits the phantom, its position, direction, and energy are saved to

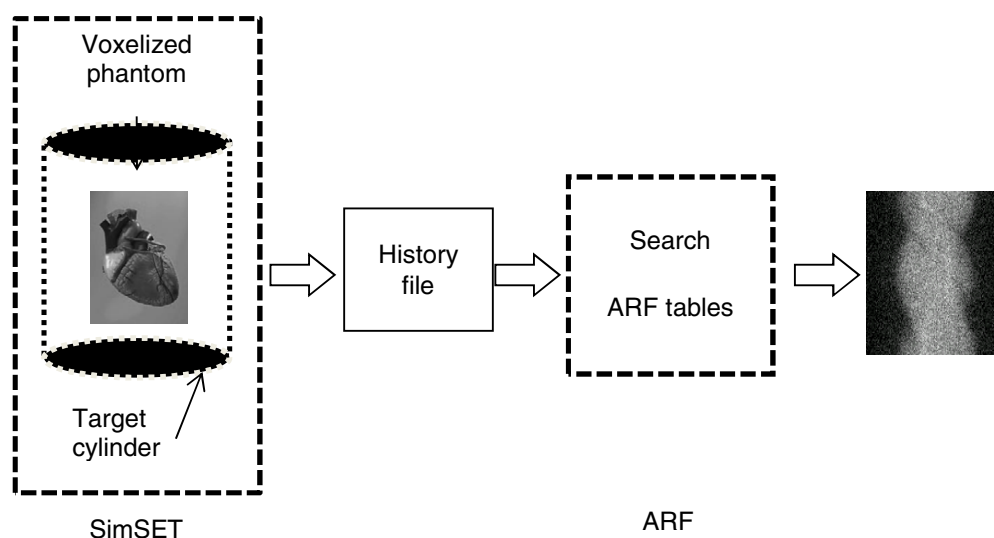


Figure 1. Block diagram of the SimSET+ARF simulation.

a history file. The history file is then processed by the ARF simulation to model interactions inside the collimator-detector system and the final projection data is generated as shown in figure 1.

The combined SimSET+ARF simulation method has been previously validated for various camera systems and a variety of radionuclides. In the original work by Song *et al* (2005), they validated the SimSET+ARF method by comparing the simulated projections with those simulated using full MC simulations using SimSET and MCNP codes (Du *et al* 2002, Wang *et al* 2002), a combination that has been validated against experimental measurements. The investigated cases were ones where interactions in the collimator-detector system are important. The SimSET+ARF combination was validated for simulation of Tc-99m/Tl-201 dual isotope cardiac imaging (where Pb x-rays fluorescence is important and the same isotope combination used for this work) and I-123/Tc-99m dual isotope brain imaging (where collimator scatter, septal penetration and partial deposition in the crystal are important interactions). They also validated it for In-111 imaging where septal penetration and scatter are non-negligible and potentially important. They modeled a GE Millennium VG camera system and a GE low-energy high-resolution (LEHR) collimator for Tc-99m/Tl-201 and I-123/Tc-99m dual isotope imaging and a medium-energy general-purpose (MEGP) collimator for In-111 imaging.

He *et al* (2005) compared the projections of a hollow plastic sphere, filled with 231.62 MBq of In-111, inside a cold elliptical phantom filled with water with the projections simulated using SimSET+ARF. They modeled a GE Discovery VH/Hawkeye SPECT/CT system with a 2.54 cm thick crystal and a MEGP collimator. Song *et al* (2011) validated SimSET+ARF by conducting a similar experiment, but modeled a Philips Precedence SPECT/CT system and a high-energy general-purpose collimator. The results of those experiments showed that the SimSET+ARF method was in good agreement with full MC simulations and physical phantom measurements for the cases studied. It also provided a substantial reduction in the simulation computational time.

As mentioned earlier, SimSET incorporates variance reduction methods to increase the simulation efficiency. Many of these methods involve changing the weight of the simulated

Table 1. Anatomical parameters of the patient population (cm).

		Body LAT ^a	Body AP ^b	LV ^c length	LV radius	Height
Male	Mean	34.84	25.70	8.31	2.67	175.68
	Std.	2.15	2.44	0.93	0.47	6.80
	Minimum	29.40	20.00	6.60	1.90	154.94
	Maximum	38.40	31.40	11.60	4.00	187.96
Female	Mean	34.37	23.50	7.39	2.32	163.45
	Std.	3.25	2.08	0.92	0.33	7.34
	Minimum	26.70	19.60	5.70	1.60	149.86
	Maximum	40.90	28.80	10.50	3.50	177.80

^a LAT: Lateral dimension.^b AP: Antero-posterior dimension.^c LV: Left ventricle.

photons. As a result, the resulting projections no longer have Poisson-distributed noise. For this reason, an alternative strategy was used to generate noisy projection data. Projections were simulated using a large number of photons in order to generate low noise projection data. A Poisson distributed pseudo random number generator (RNG) was then used to simulate the desired level of Poisson noise.

We denote the noise in the projection image from the MC simulation as MC noise. The MC noise in a given projection bin is proportional to \sqrt{N} , where N is the number of simulated photons. It thus requires a large increase in the number of simulated photons to generate low noise projection data and make a substantial decrease in the MC noise level. To make simulation of the phantom population computationally feasible, it is desirable to track as few photon histories as necessary. However, if too few photons are used to simulate the low noise projections, then after simulating Poisson noise the projections will have a higher variance than appropriate for the given count level. We thus investigated the effect of noise in the MC simulated images. We adapted and used a criterion based on the relative Poisson effective count level (He *et al* 2010) to determine the required number of simulated photons for each simulated organ. This technique provided a quantitative estimate of the true noise in the simulated projection data, including residual MC simulation noise.

Another technique that we used to make the phantom library general and the simulation computationally feasible was to simulate the organs separately. We divided each phantom into seven organs, simulated each separately. This enabled modeling of organ uptake variability by scaling and summing the projection data from the individual organs. Also, we separately simulated perfusion defects at different locations in the myocardial wall. To generate a projection image with a defect, the defect projection image was subtracted from the defect free projection prior to simulating noise (He *et al* 2004).

2. Methods

2.1. Population of realistic digital phantoms

We developed a digital phantom population that realistically and accurately models a patient population. The population included three variations each in body size, heart size, and subcutaneous adipose tissue level, for a total of 27 phantoms of each gender. The simulated population is based on the 3D XCAT phantom with organ parameters sampled from the Emory PET Torso Model Database, which contains the anatomical measurements of 166 patients who underwent cardiac imaging. Table 1 shows the relevant anatomical parameters of the patient population for male and female populations.



Figure 2. Sample transaxial slice of the background, heart, blood pool, liver, lung, kidneys and the gall bladder (from left to right) of phantom.

In this work, we used a set of user-controllable parameters (Segars *et al* 2010) to vary the anatomy of the XCAT phantom. By changing these parameters, different inner core body sizes, left ventricle (LV) length and radius and subcutaneous adipose tissue thicknesses, were simulated.

To model variation in body size, the torso and the organ sizes of the 3D XCAT phantoms were scaled to match patients with average sizes and with sizes 2 standard deviations above and below the average, based on the data from the Emory Cardiac Database. Variability in the subcutaneous adipose tissue level was modeled by scaling the XCAT skin layer by the factors 0.5 and 1.5 of the average skin layer thickness for the given body size. We kept the ratio of the average body lateral to antero-posterior dimensions fixed to 1.36 and 1.47 for male and female populations, respectively, as observed in the male and female patient populations. Variability in heart size was modeled by changing the LV length and radius while keeping their ratio fixed to 3.2 and 3.17 for the male and female population, respectively, matching the observed measurements in the patient databases.

We modeled small, medium and large hearts for each of the body sizes. To do so, we varied the heart size in terms of the LV length and radius as a function of the different body sizes. For example, a medium sized heart in a medium sized phantom was larger than a medium sized heart in a small sized phantom and smaller than that in a large sized phantom. The heart parameters were scaled to match patients with average heart sizes and with sizes that were one standard deviation above and below the average.

Each phantom was digitized prior to simulation into 0.22-cm voxels in a $256 \times 256 \times 228$ matrix. The range of the axial dimension varied such that we included 20 cm above and 30 cm below the centroid of the heart. We also checked each phantom visually to ensure that there was no unrealistic protrusion of organs into each other.

In addition to the anatomical variations, we varied the organ uptakes by dividing each phantom into seven ‘organs’, i.e., heart, liver, lungs, kidneys, gall bladder, blood pool, and the rest of the body (background). Figure 2 shows sample transaxial slices of the different organs in the phantom. We simulated projections of each organ separately assuming a homogeneous distribution inside. As described below, this enabled generation of the projection data corresponding to different organ uptakes by scaling and summing the projection data from the individual organs. It also enabled independently varying the number of photons used to simulate each organ in order to increase the simulation efficiency.

2.2. Simulate projection data using SimSET+ARF

We used the SimSET MC code in conjunction with the ARF method to generate projection images of the phantom population. This combination provides fast and accurate simulation of the SPECT system and includes modeling of septal penetration, Pb x-rays and scatter. SimSET does not provide a model of camera dead-time. Since dead-time effects are generally small for myocardial perfusion imaging, it was thus not modeled in this work.

The SimSET MC software requires two different distributions: the activity distribution and the material distribution. The activity distribution specifies the concentration of radioactive isotope in each voxel. We simulated photons with an energy of 140.5 keV for Tc-99m; for Tl-201, we simulated photons with energies of 167.4, 135.3, 82.6, 80.3, 79.9, 70.8 and 68.9 keV, where the number of photons simulated for each energy was proportional to their abundances. In SimSET, the material (e.g., tissue type) in each voxel is specified via a pointer to a list of supported materials. The supported materials include materials used in scanners or phantoms (e.g., lead, scintillation crystals, and water) and tissue types (e.g., brain, blood, bone). To better model the interactions inside the body, we added new tissue types to the SimSET material tables including ribs, cartilage, kidneys, pancreas, bone marrow, spleen, thyroid and spine. The densities and the tissue compositions were taken from the International Commission on Radiation Units and Measurements (ICRU) report 46.

We modeled a GE Infinia dual-head SPECT system with two large field-of-view scintillation cameras each fitted with a GE LEHR collimator. We modeled a 9.5 mm thick NaI(Tl) crystal within the scintillation camera with perfect energy resolution. We generated ARF tables for 1 keV wide energy windows from 48 to 140.5 keV for Tc-99m and from 48 to 167.4 keV for Tl-201. As a result, by appropriately weighting and summing these 1 keV wide projections we can model any desired energy resolution and energy window only by reprocessing the simulated projections. We created four separate sets of projection data corresponding to the detected photons that did and did not interact in the body and the collimator-camera system. This enables evaluation of the effects of the different components of the projection image on the final image quality.

In each case, the ARF tables were pre-computed using the methods described in (Song *et al* 2005). Since the photons may undergo scattering in the phantom, the energies of the photons incident on the collimator can have any values below the emission energy. We broke down the expected incident photon energies into sub-ranges and computed separate ARF tables for primary photons and for scattered photons with energies in each sub-range. These latter ARFs were used to model collimator interactions for photons scattered in the body and incident on the collimator with a lower energy. The primary photons were processed using an ARF computed using point sources with the photopeak energies mentioned above for Tc-99m and Tl-201. The scattered photons were processed by using ARFs computed using sources emitting with a uniform distribution of energies in 10 keV wide energy sub-ranges spanning the range from 40 to 140 keV for Tc-99m and from 40 to 167 keV for Tl-201. These ARF tables were then used in the ARF-based simulations to generate projection data. The projection data were generated with a 0.44 cm bin size at 120 views over 180° using a non-circular body-contouring orbit.

2.3. Relative poisson effective count level

As mentioned earlier, for MC-based simulated projections, the noise in a projection bin is proportional to the square root of the number of simulated photons (note: it is not equal to the square root of the intensity in a bin because of the use of variance reduction techniques). Figure 3 illustrates the concept of the MC residual noise in the low noise projections using an increasing number of simulated photons. It is clear that a large increase in the number of photons is required to make a significant impact on the MC noise level.

Our ultimate goal is to generate projection data with Poisson noise. One approach is to simulate projections using a very large number of photons in order to obtain an essentially noise-free estimate of the projection and then simulate Poisson noise using a Poisson pseudo-random number generator. It is desirable to be able to quantify the effects of the residual

Table 2. Relative Poisson effective count level values for the different organs for Tc-99m and Tl-201 simulation.

	Heart	Liver	Lung	Gall bladder	Kidney	Blood pool	Background
Tc-99m	0.98	0.95	0.97	0.85	0.85	0.99	0.85
Tl-201	0.99	0.98	0.99	0.98	0.9	0.99	0.9

noise on the final projection data. To do this we introduce the concept of the relative Poisson effective count level.

The relative Poisson effective count level (r_{eff}) is defined as the ratio between the Poisson variance, σ_p^2 , for a given count level and the total variance, σ_T^2 , including the variance contributions from the simulated projection (residual noise from the MC procedure) and the Poisson RNG. Ideally the projection data from the simulation would have an r_{eff} of 1. However, this would require simulating a very large number of photons. An expression for r_{eff} was derived in (He *et al* 2010) and is given by:

$$r_{\text{eff}} = \frac{\sigma_p^2}{\sigma_T^2} = \frac{s\bar{p}_s}{s^2\sigma_{\bar{p}_s}^2 + s\bar{p}_s}, \quad (1)$$

where \bar{p}_s is the mean projection image using M batches of simulated photons, $\sigma_{\bar{p}_s}^2$ is the variance of the mean projection image, \bar{p}_s , and s is the scaling factor needed to scale this simulated projection data so that it has a clinically realistic count level. We note that the variance due to the MC procedure in the simulated projections is equal to the variance before scaling, $\sigma_{\bar{p}_s}^2$ times s^2 , and the variance due to the RNG is equal to the count level, $s\bar{p}_s$.

In MC simulations, it is desirable to run the simulation multiple times using different random seeds to generate independent sequences and thus independent simulated projection images. We calculated the mean projection image \bar{p}_s and its variance $\sigma_{\bar{p}_s}^2$ using M ensembles of MC simulated projection images p_s^i . Each projection image p_s^i was simulated using a batch of 50 million photons

$$\bar{p}_s = \frac{1}{M} \sum_i p_s^i, \quad (2)$$

$$\sigma_{\bar{p}_s}^2 = \frac{1}{M^2} \text{var} \left(\sum_i p_s^i \right) = \frac{1}{M} \sigma_{p_s^i}^2. \quad (3)$$

To determine the required number of batches of photons to achieve a given r_{eff} , the expression in (1) can be written in terms of M as:

$$M = \frac{s r_{\text{eff}} \sigma_{p_s^i}^2}{\bar{p}_s (1 - r_{\text{eff}})}, \quad (4)$$

and thus the total number of photons required is equal to M times 50 million photons.

To make the simulation of the population computationally feasible and achieve acceptably low noise levels in the heart region of the projection image, we set the r_{eff} of the different organs to the values shown in table 2.

The choice of the particular r_{eff} values was somewhat empirical. Quantitatively, the effect can be understood in terms of the value itself: the total variance is $1/r_{\text{eff}}$ higher than the desired Poisson variance. The particular choice of r_{eff} was made based on a combination of qualitative, quantitative, and practical considerations. In fact, the advantage of r_{eff} is that it shows how much computational effort is needed to provide a given amount of additional quantitative advantage. Correlating the quantitative values to visual quality of the projections is somewhat

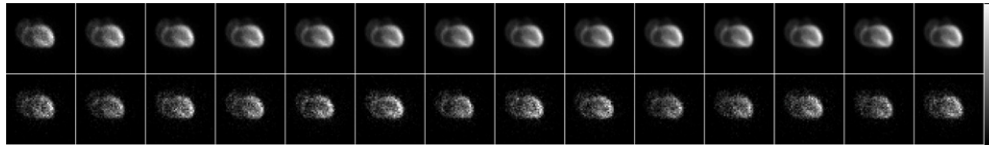


Figure 3. MC simulated anterior projections of the heart using 2, 4, 6, 8, 10, 12, 14, 16, 18, 20, 22, 24, 26 and 28×10^8 photons (top row from left to right) and the corresponding projections after adding Poisson noise (bottom row).

Table 3. Mean square difference between the heart projection images with various r_{eff} and the projection image with $r_{\text{eff}} = 0.99$.

r_{eff}	0.881	0.934	0.954	0.965	0.972	0.976	0.98	0.982	0.984	0.986	0.987	0.988	0.989
MSD	1.06	0.48	0.3	0.2	0.14	0.11	0.09	0.06	0.05	0.03	0.02	0.01	0.01

subjective. To give a better idea of how r_{eff} relates to the visual image quality, projection images shown in figure 3. Correspond to the 13 r_{eff} values indicated in table 3 plus $r_{\text{eff}} = 0.99$. Table 3 also gives the mean square difference (MSD), in units of square counts, between projections of the heart of a medium sized male phantom with various r_{eff} values compared to the projection with the $r_{\text{eff}} = 0.99$.

2.4. Modeling energy resolution

As mentioned earlier, projections were generated assuming a perfect detector (i.e., energy resolution equal to zero) to allow modeling of any arbitrary energy resolution. Also, they were generated in 1 keV wide energy bins so they could be combined to permit study of the effects of window width. Energy resolution was modeled at the time the windows were combined to form an acquisition energy window in order to allow studying the optimal energy windows as a function of energy resolution.

For any arbitrary acquisition energy window, $ewin$, and detector with energy resolution, $eres$, we model a projection image (p_{ewin}^{eres}) as

$$p_{ewin}^{\text{eres}} = \sum_{e=48}^{184} w_e^{\text{eres}} p_e, \quad (5)$$

where w_e^{eres} denotes the probability that an incident photon with an energy e would be detected in an energy window e for a detector with energy resolution $eres$, and p_e is the simulated projection image acquired in an energy window $(e, e+1)$ using a detector with perfect energy resolution.

Detectors with arbitrary energy response functions can be modeled using equation (5). For scintillation crystals such as NaI(Tl) and LaBr, the energy response can be modeled as a Gaussian function with a specified per cent energy resolution at 140.5 keV and an inverse square root energy dependence. For this model there is an analytic expression for w_e^{eres} . However, for detector materials such as CZT detectors, where the energy response is non-Gaussian, we developed an analytical model of the CZT energy response from which we could compute w_e^{CZT} .

The model of CZT energy spectral includes three parts: the charge induction efficiency as a function of depth of interaction, the probability that a gamma photon deposit its energy as a function of depth, and a Gaussian distribution of the generated charge carriers (LeClair *et al* 2006).

When a gamma photon with energy E_0 deposits its energy in a CZT detector at depth x it will generate N electron-hole pairs, where $N = E_0/e$ and e is the pair creation energy of the CZT detector (~ 4.64 eV). When a bias potential is added to the detector the electrons and holes will move toward and induce charges on the anode and cathode, respectively. The efficiency of the charge induction (or the fraction of charge collected) is given by the Hecht relation:

$$\eta(x) = \frac{\lambda_e}{D} (1 - e^{-(D-x)/\lambda_e}) + \frac{\lambda_h}{D} (1 - e^{-x/\lambda_h}) \quad (6)$$

where, D is the detector thickness, λ_e is the mean free path of electrons, and λ_h is the mean free path of holes. The two mean free paths are related to the bias potential and characteristics of the detector material.

The detected gamma photon energy is proportional to the number of charges collected, therefore:

$$E(x) = \frac{\eta(x)}{\eta(x=0)} E_0. \quad (7)$$

Assuming that all the gamma photons are absorbed at the first interaction site in the detector, the probability that a gamma photon with energy E_0 deposits its energy in the CZT detector at depth x is given by Beer's law:

$$P(x) = \mu(E_0) e^{-\mu(E_0)x} dx. \quad (8)$$

Here $\mu(E_0)$ is the linear attenuation coefficient of the detector material at energy E_0 .

Also, due to counting statistics the final detected energy is Gaussian distributed and centered at $E(x)$ and has a variance E . The FWHM (in units of energy) of this Gaussian distribution is given by:

$$\text{FWHM}_{E(x)} = 2.3548 \eta(x) \sqrt{F \varepsilon E_0} \quad (9)$$

where F is the *Fano* factor, accounting for the difference between the observed energy resolution and that resulting from Poisson counting statistics (Cherry *et al* 2012, Knoll 2010).

Based on this, we have the detector spectrum at energy E for gamma photon deposited at depth x as:

$$S(E, x) = \mu(E_0) e^{-\mu(E_0)x} \text{Gaussian}(E(x), E) dx. \quad (10)$$

Integrating the above over the entire detector thickness, D , we then have that the detected energy spectrum, $s(E)$, is given by:

$$S(E) = \int_0^x \mu(E_0) e^{-\mu(E_0)x} G(E(x), E) dx \quad (11)$$

or as a discrete approximation:

$$S(E) = \sum_{i=0}^L \mu(E_0) e^{-\mu(E_0)x_i} G(E(x_i), E) \Delta x. \quad (12)$$

$x_i = i * \Delta x$

Based on above model, we calculated the energy spectrum for Tc-99m detected in a 5 mm thick CZT detector system with ~ 500 V bias potential. Figure 4 shows the good agreement between the measured and calculated spectra based on the model. Note the peak at 40 keV is from a characteristic x-ray of the CZT that is not included in the model.

Figure 5 shows the detection probability of a photon in a 20% wide acquisition energy window centered at 140.5 keV for three different detectors as a function of the photon's energy. For the case of ideal detectors, all photons with energies within the energy window range are counted. For detectors with a Gaussian energy response, such as NaI(Tl) crystals, notice the symmetric distribution of the photons detected in the acquisition energy window. However, for

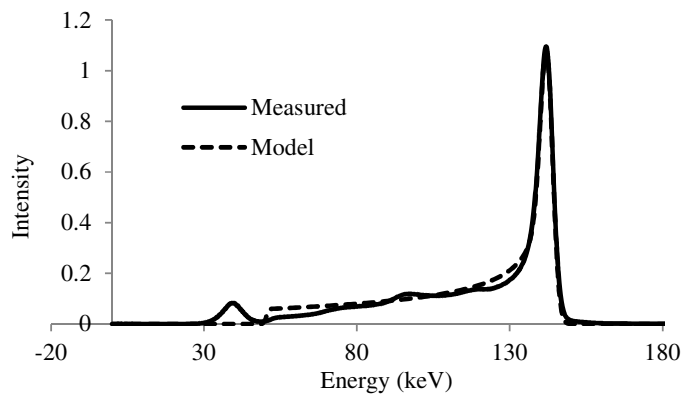


Figure 4. Comparison between measured and calculated spectrum of Tc-99m.

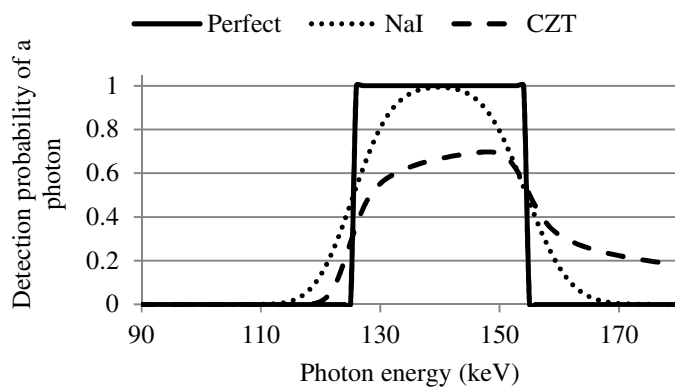


Figure 5. Detection probability of photons for a perfect, NaI(Tl) crystal and CZT detector in a 20% wide acquisition energy window centered at 140.5 keV.

CZT detectors, it is quite clear the asymmetric distribution of the detection probability results from the tail of the energy resolution function.

2.5. Validation of the energy window and energy resolution modeling method

The proposed simulation approach used the SimSET MC code and ARF tables to model the interactions inside the body and collimator-detector system respectively. ARF tables were generated assuming a perfect detector system into 1 keV wide bins. Finally, the acquisition energy window and the detector energy resolution were modeled by appropriately weighting and summing the 1 keV wide projections using equation (5). The former simulation tools have been extensively validated as mentioned earlier. However, the method of modeling the energy window and resolution has not been validated yet.

We validated the proposed method by comparing projections generated using equation (5) with those simulated using pre-generated ARF tables that include models of the energy window and resolution. We computed the per cent average absolute difference for the projection images of the different organs using both methods. We investigated acquisition energy window widths of 10%, 20% and 40% centered at 140.5 keV for Tc-99m modeling a NaI(Tl) scintillation crystal. For each organ, the number of simulated photons corresponded to the r_{eff} values as given in table 2.

Table 4. Activity parameters of Tc-99m and Tl-201.

Activity (counts cm ⁻³)	Mean		Std. deviation		Minimum		Maximum	
	Tc-99m	Tl-201	Tc-99m	Tl-201	Tc-99m	Tl-201	Tc-99m	Tl-201
Heart	9139	3090	2625	605	4774	2030	15 716	4118
Liver	3852	1994	2362	680	709	1099	10 061	4071
Lung	843	396	330	105	408	255	1957	658
Gall bladder	80 299	668	63 726	286	10 234	379	279 583	1540
Kidney	13 208	6438	5391	1528	6086	3629	24 750	9741
Blood	731	668	360	286	234	379	2011	1540
Background	731	668	360	286	234	379	2011	1540

2.6. Modeling uptake variability

For each phantom in the population, we simulated low noise Tc-99m and Tl-201 projection data for the heart, liver lung, gall bladder, kidney, blood and background (including all other organs). By doing so, we could generate a projection image of the entire phantom for any relative uptake value in these organs and product of injected activity and acquisition duration by scaling and summing these individual sets of projection data followed by simulating Poisson noise. Variations in organ uptake were modeled by randomly sampling the scale factors from truncated Gaussian distributions with parameters as shown in table 4. The distributions were based on data from a set of 34 patients who underwent dual isotope myocardial perfusion studies. Patients were injected with 30 mCi of Tc-99m and 4 mCi of Tl-201 following a standard clinical protocol.

3. Results

3.1. Population of realistic digital phantoms

Figure 6 to figure 8 show sample coronal and transaxial images of attenuation distributions illustrating variations in body size, heart size and subcutaneous adipose tissue thickness of the population.

3.2. Simulated projection data using an efficient Monte Carlo method

For each phantom and organ we calculated the required number of simulated photons using equation (4). Figure 9 shows sample low noise projection images using r_{eff} values from table 2.

We validated the method for simulating data for an arbitrary energy window and resolution by comparing projections generated using equation (5) with those simulated using ARF tables where the energy window and resolution were modeled when generating the ARF tables, as has been used and validated in previous work. The same exact set of photons exiting the body was used to generate both projections. Figure 10 shows the projection image of the different organs generated using both methods. We computed the per cent average absolute difference (table 5), defined as the absolute value of the pixel-by-pixel difference in projections, summed this over all projection bins, and divided this by the average of the sum of the two projections. Using the absolute value prevents cancellation of errors with different signs in the sum, and summing before dividing by the mean prevents voxels with very small values from dominating the error metric. The average absolute per cent difference was always less than 0.1% and was generally substantially smaller than this.

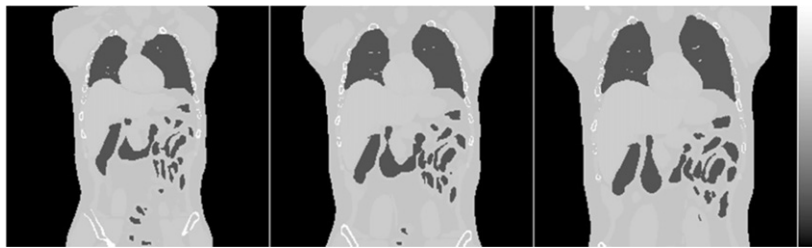


Figure 6. Sample coronal images of the attenuation distribution from the male phantom population showing variations in body size for a medium heart size and average subcutaneous adipose tissue thickness.



Figure 7. Sample coronal images of attenuation distribution from male phantom population showing variations in subcutaneous adipose tissue thickness for medium body and heart sizes.

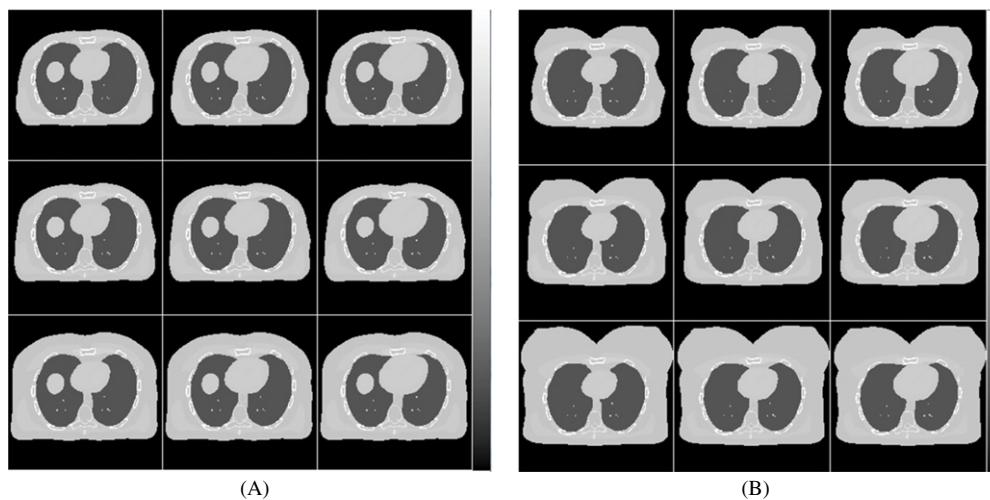


Figure 8. Sample transaxial images of the attenuation distribution from male (A) and female (B) phantom populations showing variations in heart size (left to right) and subcutaneous adipose tissue thickness (top to bottom) for a medium body.

Some difference in the two methods is expected due to differences in the way the effect of energy resolution and the collimator-detector response function (CDRF) are modeled in the two methods. In particular, when using data from 1 keV wide bins the energy resolution and the probabilities of counting photons in a given energy window were calculated based on the energy value at the center of each energy bin. On the other hand, when the energy resolution

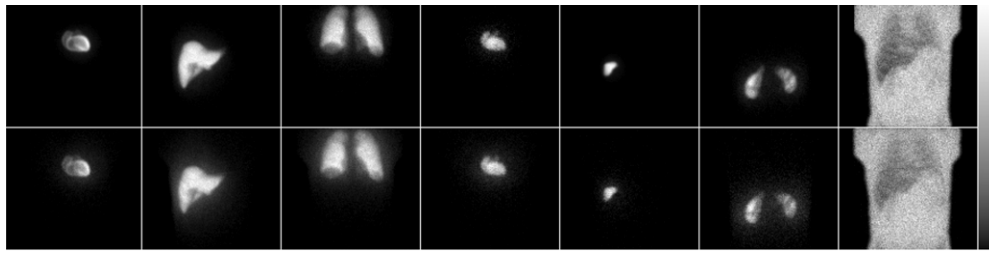


Figure 9. Low noise projection images of Tc-99m (top row) and Tl-201 (bottom row) of a medium sized phantom. Projection images were acquired in a 20% acquisition energy window centered at 140.5 keV for Tc-99m and 30% acquisition energy window centered at 72 keV for Tl-201.

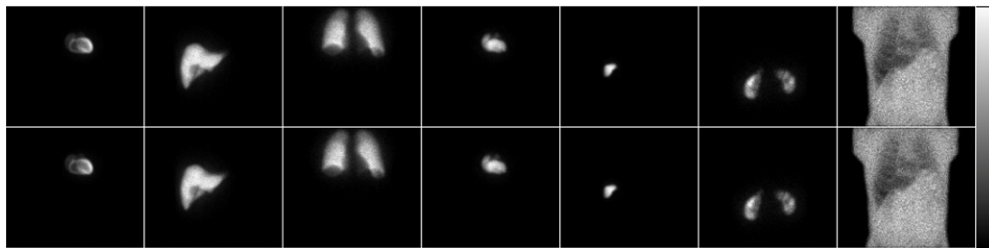


Figure 10. Low noise projection images of the different organs for a medium sized phantom for Tc-99m acquired in a 20% acquisition energy window centered at 140.5 keV. Energy window and resolution are modeled using equation (5) (top row) and inside the ARF (bottom row).

Table 5. Per cent average absolute difference of projection images for the different organs.

Energy window width/organ	Heart	Liver	Lung	Blood pool	Gall bladder	Kidney	Background
10%	0.003	0.003	0.003	0.003	0.003	0.003	0.004
20%	0.007	0.007	0.007	0.007	0.008	0.007	0.008
40%	0.084	0.079	0.085	0.081	0.087	0.079	0.092

was included in the ARF, it was modeled for each photon energy when generating the ARF. In addition, the effects of the CDRF were averaged over the window by sampling photon energies from a uniform energy distribution spanning the range of the ARF energy window. Thus, the method of including energy resolution assumes that the CDRF is energy invariant over a larger range of energies than the method using 1 keV bins. This latter effect explains the increasing percentage difference with increasing energy window width.

As mentioned earlier, we generated separate sets of projection data for each of the four categories of detected photons, i.e., (A) photons that did not interact inside the body or the collimator, (B) photons that did not interact inside the body but interacted in the collimator, (C) photons that interacted inside the body but did not interact in the collimator, and finally (D) those that interacted inside the body and the collimator. Figure 11 shows the different sets of projections.

Figure 12 shows sample noisy projection images modeling uptake and anatomical variations by scaling and summing the individual organ projections using scale factors

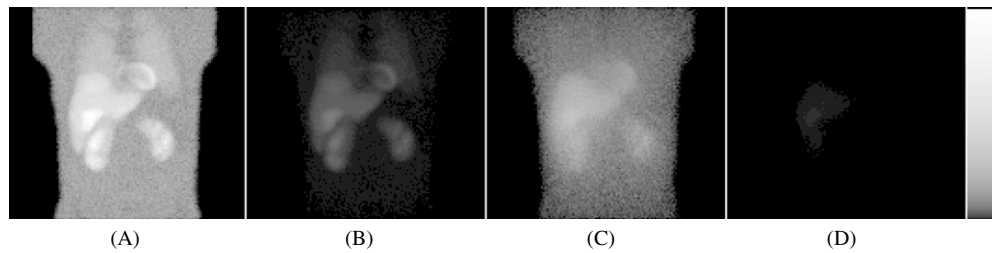


Figure 11. Low noise Tc-99m images for the different components of the projection. The components are: (A), (B), (C), and (D). Images were displayed using a logarithmic gray scale to better show the lower uptake organs.

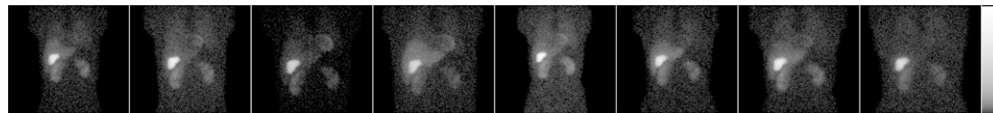


Figure 12. Sample Tc-99m noisy projection images modeling anatomical and uptake variations acquired in a 20% acquisition energy window width. Images were displayed using a logarithmic gray scale to better show the lower uptake organs.

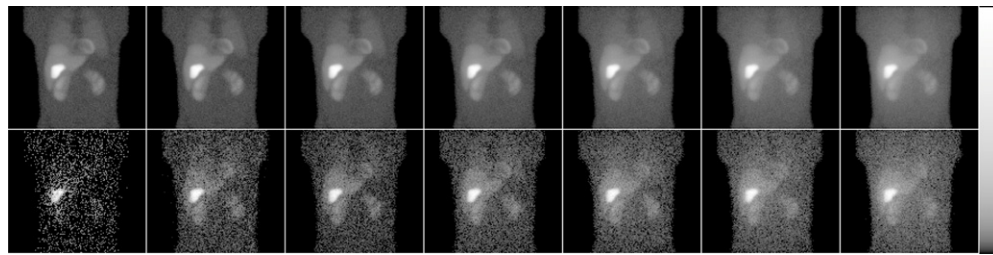


Figure 13. Sample of low noise (top) and noisy (bottom) MC simulated projection images of a medium sized male phantom with medium size heart and average subcutaneous adipose tissue thickness acquired from an anterior projection view in energy windows with widths of 1, 9, 25, 37, 57, 77 and 101 keV centered at 140.5 keV from left to right respectively. Images were displayed using a logarithmic gray scale to better show the lower uptake organs.

randomly sampled from the corresponding truncated Gaussian distribution with parameters shown in table 4.

3.3. Applications

In the context of MPS, one application would be finding the optimum Tc-99m or Tl-201 acquisition energy window width. To do that, we will have to generate projection images acquired in various acquisition windows. By applying the above-described methods of modeling the energy window and resolution, we can generate the projection images in any arbitrary energy window and resolution quickly and easily.

Figure 13 shows sample low noise and noisy projection images simulated for various energy windows. Note the tradeoff between increasing scatter, which reduces the contrast of the myocardium, and noise as the energy window width increases. Figure 14 shows sample noisy Tc-99m projection images for a medium sized phantom acquired from anterior projection view for different energy windows using a perfect detector, NaI(Tl) crystal and CZT detector.

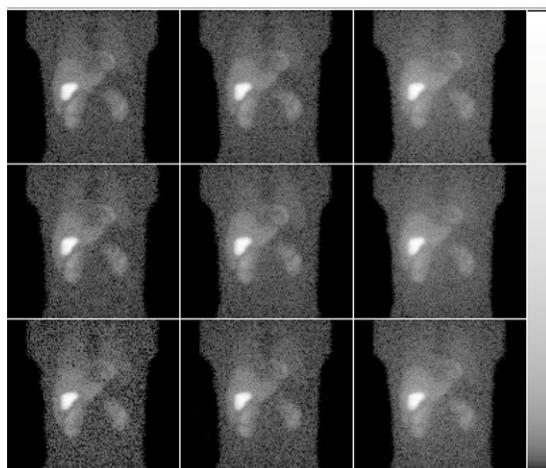


Figure 14. Sample noisy Tc-99m projection images for a medium sized phantom acquired from an anterior projection view in 10%, 20% and 40% wide energy windows (from left to right) using a perfect detector, NaI(Tl) crystal with 9% energy resolution and CZT detector (from top to bottom, respectively). Images were displayed using a logarithmic gray scale to better show the lower uptake organs.

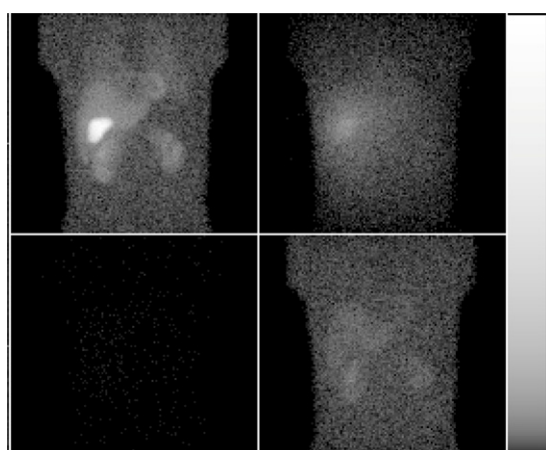


Figure 15. Sample noisy projection images for Tc-99m (top row) and Tl-201 (bottom row) acquired in a 20% acquisition energy window (left) centered at 140.5 keV and 30% acquisition window (right) centered at 72 keV using a NaI(Tl) crystal with 9% energy resolution. Images were displayed using a logarithmic gray scale to better show the lower uptake organs.

Another application of interest is the optimization and evaluation of the simultaneous stress Tc-99m/rest Tl-201 dual isotope cardiac SPECT protocol. Crosstalk contamination, where photons emitted by Tc-99m contribute to the Tl-201 image due to interactions in the patient and gamma camera, degrades image quality. Figure 15 demonstrates the effect of the down scatter component from Tc-99m into a Tl-201 energy window. Note the negligible contribution of Tl-201 to the Tc-99m energy window. Reducing the amount of crosstalk by optimizing energy windows settings and relative injected activities could reduce the impact of crosstalk and improve the image quality. The flexible design of the projection database allows

Table 6. Comparison of CPU time for simulation of Tc-99m using SimSET + ARF.

	SimSET + ARF	SimSET + ARF 'standard'
Number of photons	50 million	50 million
SimSET	~55 min	~55 min
ARF	~285 min	~32 min
Overhead time ^a	~2 min	0

^a Overhead time includes the time taken to sum the individual 1 keV projection images to generate a projection image for a given energy window and resolution combination.

us to generate rapidly projections for various combinations of Tc-99m and Tl-201 acquisition windows.

3.4. Computational efficiency

The generation of projection data for each complete phantom realization required 14.8 CPU years and 48 GB of disk space. This represents a total of 799 CPU years and 2.6 TB of disk space for the entire phantom population. The CPU times are for a single core of a 2.33 GHz Intel Xeon E5410 quad core processor. A breakdown of the simulation times of one batch of simulated photons is shown in table 6. Note that for these simulations most of the processing time is taken in the ARF code, which models the interactions inside the collimator and detector system. This is because we generated projection images in 1 keV energy bins. We ran a simulation using SimSET+ARF where we modeled the acquisition energy window and resolution in the ARF tables prior to the simulation. We call this simulation the 'Standard' method. We see that the simulation time is less by a factor of 4 than our simulation time. However, when investigating multiple combinations of windows and resolutions as in (Ghaly *et al* 2012, 2013), where a total of 13 energy windows and 3 energy resolutions were investigated, the 'Standard' SimSET+ARF method would have taken ten times longer than the proposed method.

4. Discussion

This paper presents a methodology for the design and simulation of a digital phantom population for use in myocardial perfusion SPECT research. The population included variability in gender, body size, heart size and fat level with no modeling of the cardiac or respiratory motion included. The major application of the specific data set generated here was focused on the energy dimension, because of our interest in dual isotope imaging. For this application, choosing optimal energy windows is important. The energy dimension is also important for investigating the potential improvement in image quality provided by detectors with improved energy resolution. Since we were primarily interested in comparing scatter and crosstalk compensation methods and optimizing energy windows, respiratory and cardiac motions would impact all methods equally and tend to result in a general reduction in performance. On the other hand, uptake distribution and organ geometry result in different degrees of scatter and crosstalk artifacts. Previous results have indicated the importance of including anatomic and uptake variability (He *et al* 2004), and there is certainly the potential for different energy windows or compensation methods to perform differently with different anatomies and uptakes. In an attempt to acknowledge the fact that the heart changes shape during beating motion, we did generate the phantoms at the point in the cardiac cycle where the heart was closest to the average of the heart over the eight gates of the cardiac cycle.

Adding the time dimension (motion) to the simulations would require a substantial increase in computational complexity. With current MC simulations this would require simulating data

at multiple points in the cardiac and respiratory cycle. Since these motions are not synchronous, this involves simulating all possible combinations. For example, using eight phases each for cardiac and respiratory phases would increase the computational complexity by a factor of 64. If the images were ultimately to be added together, the simulation time would of course not be increased by this factor to obtain an equal noise level. However, the amount of disk space, number of simulations, etc, would all be increased. However, in principle the methodology described in this paper could be extended to include motion without difficulty beyond the increased computational complexity.

One other aspect of the clinical situation that is not modeled is the effect of the various data corrections. These include energy, spatial, and linearity corrections as well as corrections for center of rotation. In modern gamma cameras these corrections are implemented during the acquisition process or prior to image reconstruction, and the raw projections given to the user often include them. In previous studies, our reconstruction codes, which do not implement these corrections, have provided accurate reconstructions with good image quality. We have observed this for radionuclides as diverse as Tc-99m (Song *et al* 2004), In-111 (He *et al* 2005), I-131 (Song *et al* 2011), and Y-90 bremsstrahlung photons (Rong *et al* 2012). As a result, we believe that residual correction errors are small compared to other effects. A related effect that is not modeled in this work is the potential change in noise characteristics that these methods might introduce. However, once again this effect is likely small compared to the quantum noise level itself. Thus we believe these effects can safely be neglected for the simulation applications of interest here, as they have been in essentially all nuclear medicine simulations we are aware of to date.

The combination of the methods used allowed us to efficiently simulate realistic projections for a realistic population of phantoms. The population is useful for performing rigorous and comprehensive optimization and evaluation of the instrumentation, acquisition and reconstruction/compensation methods in the context of MPS imaging. We have already used the phantom population and the simulated projection images to find the optimal Tc-99m acquisition energy window and investigated the effects of energy resolution on the image quality using the ideal observer (IO) and the recently developed IO with model mismatch in the context of a myocardial perfusion SPECT defect detection task (Ghaly *et al* 2012, 2013). Finally we have also investigated the optimal acquisition energy window and relative injected activity in the context of dual isotope MPS (Ghaly and Frey 2011).

5. Conclusion

There is an increasing need to perform initial validation, optimization, and evaluation of nuclear medicine imaging methods using realistic simulations. Such simulations must realistically model the clinical situation, including patient populations and clinical imaging systems. Technologies for generating realistic phantoms and modeling imaging systems have previously been developed. However, modeling populations of phantoms and providing the ability to evaluate parameters such as energy window and energy resolution function, acquisition time, and administered activity requires combining multiple technologies. In addition, despite increases in available computer processing speed, careful implementation is needed for the simulations to be computationally feasible.

We have developed a comprehensive method for efficiently simulating such a population in the context of myocardial perfusion imaging. The set of digital phantoms, the simulation methods themselves, and the set of simulated MPS projections provide tools and methods needed to expand the applications of realistic simulation in the optimization and evaluation of nuclear medicine and SPECT imaging.

References

- Barclay A B, Eisner R L and DiBella E 2005 PET thorax model database
- Cherry S R, Sorenson J A and Phelps M E 2012 *Physics in Nuclear Medicine* (Philadelphia, PA: Elsevier)
- Du Y, Frey E C, Wang W T, Tocharoenchai C, Baird W H and Tsui B M W 2002 Combination of MCNP and SimSET for Monte Carlo simulation of SPECT with medium- and high-energy photons *IEEE Trans. Nucl. Sci.* **49** 668–74
- Fung G S K, Segars W P, Lee T-S, Higuchi T, Veress A I, Gullberg G T and Tsui B M W 2010 Realistic simulation of regional myocardial perfusion defects for cardiac SPECT studies *NSS/MIC'10: IEEE Nuclear Science Symp. Conf. Record* pp 3061–4
- Funk T, Kirch D L, Koss J E, Botvinick E and Hasegawa B H 2006 A novel approach to multipinhole SPECT for myocardial perfusion imaging *J. Nucl. Med.* **47** 595–602
- Ghaly M and Frey E 2011 Optimization of energy windows and injected activities for dual-isotope simultaneous-acquisition (DISA) myocardial perfusion SPECT using ideal observer (IO) and realistic background variations *J. Nucl. Med.* **52** 2014
- Ghaly M, Links J M, Du Y and Frey E 2012 Importance of including model mismatch in ideal observer-based acquisition parameter optimization in SPECT *J. Nucl. Med.* **53** 326
- Ghaly M, Links J M, Du Y and Frey E C 2013 Model mismatch and the ideal observer in SPECT *Proc. SPIE* **8673** 86730K
- He B, Du Y, Song X Y, Segars W P and Frey E C 2005 A Monte Carlo and physical phantom evaluation of quantitative In-111SPECT *Phys. Med. Biol.* **50** 4169–85
- He X, Frey E C, Links J M, Gilland K L, Segars W P and Tsui B M W 2004 A mathematical observer study for the evaluation and optimization of compensation methods for myocardial SPECT using a phantom population that realistically models patient variability *IEEE Trans. Nucl. Sci.* **51** 218–24
- He X, Links J M and Frey E C 2010 An investigation of the trade-off between the count level and image quality in myocardial perfusion SPECT using simulated images: the effects of statistical noise and object variability on defect detectability *Phys. Med. Biol.* **55** 4949–61
- Knoll G F 2010 *Radiation Detection and Measurement* (Hoboken, NJ: Wiley)
- LaCroix K J, Tsui B M, Frey E C and Jaszczak R J 2000 Receiver operating characteristic evaluation of iterative reconstruction with attenuation correction in 99 mTc-sestamibi myocardial SPECT images *J. Nucl. Med.* **41** 502–13
- LeClair R J, Wang Y, Zhao P, Boileau M, Wang L and Fleuret F 2006 An analytic model for the response of a CZT detector in diagnostic energy dispersive x-ray spectroscopy *Med. Phys.* **33** 1329–37
- Lewellen T K, Harrison R L and Vannoy S 1998 *The Simset Program* (Bristol: Institute of Physics Publishing) pp 77–92
- Rong X, Du Y, Ljungberg M, Rault E, Vandenberghe S and Frey E C 2012 Development and evaluation of an improved quantitative Y-90 bremsstrahlung SPECT method *Med. Phys.* **39** 2346–58
- Segars W P, Sturgeon G, Mendonca S, Grimes J and Tsui B M 2010 4D XCAT phantom for multimodality imaging research *Med. Phys.* **37** 4902–15
- Segars W P, Tsui B M, Lalush D S, Frey E C, King M A and Manocha D 2001 Development and application of the new dynamic Nurbs-based Cardiac-Torso (NCAT) phantom *J. Nucl. Med.* **42** 7
- Segars W P and Tsui B M W 2002 Study of the efficacy of respiratory gating in myocardial SPECT using the new 4-D NCAT phantom *IEEE Trans. Nucl. Sci.* **49** 675–9
- Segars W P and Tsui B M W 2009 MCAT to XCAT: the evolution of 4D computerized phantoms for imaging research *Proc. IEEE* **97** 1954–68
- Song N, Du Y, He B and Frey E C 2011 Development and evaluation of a model-based downscatter compensation method for quantitative I-131 SPECT *Med. Phys.* **38** 3193–204
- Song X, Frey E C, Wang W T, Du Y and Tsui B M W 2004 Validation and evaluation of model-based crosstalk compensation method in simultaneous Tc-99 m stress and Tl-201 rest myocardial perfusion SPECT *IEEE Trans. Nucl. Sci.* **51** 72–9
- Song X, Segars W P, Du Y, Tsui B M and Frey E C 2005 Fast modelling of the collimator-detector response in Monte Carlo simulation of SPECT imaging using the angular response function *Phys. Med. Biol.* **50** 1791–804
- Wang W T, Frey E C, Tsui B M W, Tocharoenchai C and Baird W H 2002 Parameterization of Pb x-ray contamination in simultaneous Tl-201 and Tc-99 m dual-isotope imaging *IEEE Trans. Nucl. Sci.* **49** 680–92